Experimental measurements of the collisional absorption of XUV radiation in warm dense aluminium

B. Kettle,[1,*] T. Dzelzainis,[1] S. White,[1] L. Li,[1] B. Dromey,[1] M. Zepf,[1] C. L. S. Lewis,[1] G. Williams,[2] S. Künzel,[2] M. Fajardo,[2] H. Dacasa,[3] Ph. Zeitoun,[3] A. Rigby,[4] G. Gregori,[4] C. Spindloe,[5] R. Heathcote,[5] and D. Riley[1]

[1]*Centre for Plasma Physics, School of Mathematics and Physics, Queen's University Belfast, University Road, Belfast BT7 1NN, United Kingdom*

[2]*Group of Lasers and Plasmas, Instituto de Plasmas e Fusão Nuclear, Instituto Superior Técnico, Universidade de Lisboa, 1049-001 Lisbon, Portugal*

[3]*Laboratoire d'Optique Appliquée, ENSTA ParisTech, CNRS, Ecole Polytechnique, Université Paris–Saclay, 828 Boulevard des Marchaux, 91762 Palaiseau Cedex, France*

[4]*Clarendon Laboratory, Parks Road, Oxford OX1 3PU, United Kingdom*

[5]*Central Laser Facility, Harwell, Oxfordshire OX11 0QX, United Kingdom*

(Received 1 February 2016; revised manuscript received 24 April 2016; published 5 August 2016)

The collisional (or free-free) absorption of soft x rays in warm dense aluminium remains an unsolved problem. Competing descriptions of the process exist, two of which we compare to our experimental data here. One of these is based on a weak scattering model, another uses a corrected classical approach. These two models show distinctly different behaviors with temperature. Here we describe experimental evidence for the absorption of 26-eV photons in solid density warm aluminium ($T_e \approx 1$ eV). Radiative x-ray heating from palladium-coated CH foils was used to create the warm dense aluminium samples and a laser-driven high-harmonic beam from an argon gas jet provided the probe. The results indicate little or no change in absorption upon heating. This behavior is in agreement with the prediction of the corrected classical approach, although there is not agreement in absolute absorption value. Verifying the correct absorption mechanism is decisive in providing a better understanding of the complex behavior of the warm dense state.

DOI: 10.1103/PhysRevE.94.023203

An important challenge for modern theoretical physics is the description of warm dense matter that is present in dense astrophysical plasmas [1,2], material science [3], and inertial confinement fusion schemes [4]. The complex nature of these energetic states stems from the coexistence of partial degeneracy, strong particle coupling, and excited electrons. However, since the bulk properties of matter are ultimately connected to the microscopic structure and dynamics, experiments measuring such properties can act as a gateway to better understanding. The collisional or inverse bremsstrahlung absorption of extreme ultraviolet (XUV) radiation by warm dense matter is one such route to uncovering properties such as the electron-ion collision rate and is a subject of great interest. Here we describe experimental evidence for the absorption of 26-eV photons in solid density warm aluminium ($T_e \approx 1$ eV). These results help distinguish between the weak scattering model of Vinko *et al.* [5] and the corrected classical model of Iglesias [6], which show distinctly different behaviors with temperature. Aluminium is an oft chosen prototypical material used to study the behavior of matter under warm dense conditions. Also, as the XUV radiation we study here lies above the aluminium plasma frequency (≈15-eV photons) yet below the L edge (72.6 eV), we are assured that free-free absorption is the dominant mechanism for transferring energy to the medium, making it a perfect candidate for testing collisional XUV absorption processes.

The experiment was performed at the Vulcan laser facility (United Kingdom) [7]. Figure 1 shows a schematic of the target setup. A submicron aluminium sample foil is supported by a thin steel frame and placed at 45° between two palladium-coated CH foils, 1 mm from each. Laser pulses of $\approx 2 \times 10^{15}$ W/cm^2 strike the palladium foils, converting the incident light energy into M-L band x rays in the 3–3.5 keV region, with an efficiency of approximately 4% [8,9]. These keV x rays are used to volumetrically heat the thin aluminium foil to create a core of solid density warm dense aluminium that can be probed by a short duration pulse of XUV light. The CH backing suppresses lower-energy photons to ensure more volumetric heating of the sample. Four crystal-based x-ray spectrometers, an x-ray pinhole camera, and an x-ray streak camera are used to characterize the keV x rays from the palladium foils. This technique rapidly deposits energy before substantial hydrodynamic expansion of the aluminium occurs and has previously been studied by Kettle *et al.* [8]. Ray-tracing simulations show that uniform solid density samples can be created, with temperatures in the warm dense matter regime and a maximum variation of ≈10% in the temperature across the sample face. The aluminium sample will have a uniform surface layer of a few nm of oxide [10] and typically a few nm of organic surface contamination [11]. In addition, despite the rapid x-ray heating, the outer edges of the aluminium foil will begin to decompress during heating. Due to these surface factors, the experiment relies upon probing different thicknesses of foil on separate shots and noting that the difference in transmission between any two samples is due solely to the additional thickness of solid density warm aluminium.

The XUV probe is generated by a synchronized short pulse laser (≈1 ps, 527 nm), which is loosely focused through an

*Corresponding author: bkettle01@qub.ac.uk

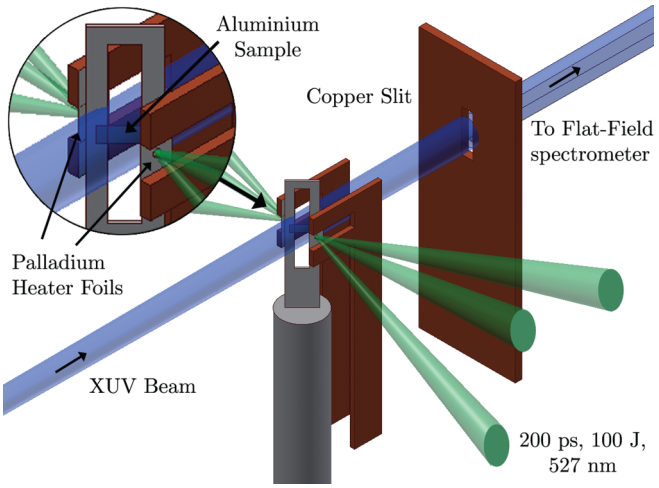

FIG. 1. Experiment setup. Two palladium-coated CH foils surround a thin submicron aluminium sample (1 mm away). Three 527-nm laser pulses provide a total of $\approx 2 \times 10^{15}$ W/cm^2 laser intensity onto each palladium foil (100 J in 200 ps full width at half maximum), which is converted into hard x rays that bathe the sample, raising its temperature. An XUV probe propagates through the heated sample and onward to a spectrometer for analysis.

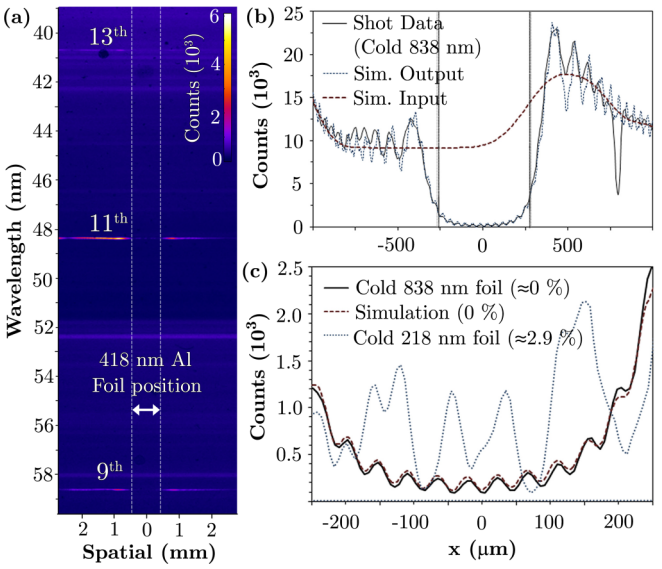

FIG. 2. (a) Spectrometer data for an XUV shot through a heated 418-nm foil, with the position of the sample foil in the spatial axis (horizontal) highlighted. The spectral dispersion in the image goes from top to bottom, with increasing wavelength (or decreasing photon energy). (b) Line out along the spatial axis of the 11th harmonic, from a shot through a cold 838-nm aluminium foil, centered at $x = 0$ (black solid line). The diffraction simulation input (red dashed line) and output (blue dotted line) are compared to these data. The position of the foil edges are highlighted with the vertical dotted lines. (c) Same shot data of (b) (solid black) compared to the source-broadened output of the diffraction simulation (red dashed line). The shot data for the 11th harmonic on a cold 218-nm foil are also included (blue dotted line) for comparison.

argon gas jet to create a bright source of high harmonics [12,13], providing discrete spectral lines of radiation in the 40–60 nm region (20–30 eV). The probe beam is P polarized with respect to the target angle and propagates through and around the sample, before being spectrally dispersed inside a flat-field grating spectrometer [14] for analysis. A copper shield restricts the probe rays to those that pass through the sample frame. It should be noted that such foil heating and XUV probing studies cannot be easily achieved on existing XUV free-electron laser experiments, which are excellent for cold matter studies.

Data from an XUV shot through a heated aluminium sample is shown in Fig. 2(a). Three harmonic orders can be seen: the 13th, 11th, and 9th (from top to bottom), with the 11th order being the brightest by a factor of nearly 4. The presence of the sample foil can clearly be seen in the center of the profile where there is a large drop in signal. Carbon emission lines from the CH backing on the palladium (in higher diffraction order) as well as low-level continuum emission background are visible, but consistent (less than 1% noise level with respect to the main signal) and easily identified for removal from the spectra. Unfortunately, due to the effects of refraction upon penetrating through the sample foil, the data from the 9th harmonic are unreliable. This is discussed later in the text.

In Fig. 2(b) an averaged line-out profile along the spatial axis is given for the 11th harmonic on a shot through an 838-nm cold aluminium sample. The sample thickness has been accurately measured by RAL Target Fabrication department using a contact probe and is known to ± 5 nm. There is evidence of diffraction effects both outside and inside the foil shadow region. Note that the drop in signal around $x = 800\ \mu$m is an artifact of the CCD. The diffraction features have been simulated with a mathematical model that allows for a nonuniform XUV profile to be incident upon the strip of aluminium foil. If the observation plane is sufficiently close to an object or aperture, we are in the near-field region and Fresnel diffraction laws apply [15,16]. This is true when $R < \frac{a^2}{\lambda}$, where a is the obstacle or aperture width and R is the smaller of the source-to-obstacle or obstacle-to-observation distances. For the experiment described here, λ is of the order of 10 s of nanometers (XUV), $R = 1$ m for the obstacle-to-observation plane (the spectrometer), and $a = 500\ \mu$m (the sample foil width); we are within the near-field regime. We are confident that the transmission of this thicker foil is known to be effectively zero (<0.1%) at this photon energy and this provides us with an unambiguous reference for testing our ability to match the measured diffraction pattern with the calculated one. All the integrated energy in the shadow region of the profile is due to diffraction from the edges. This model is applied in Fig. 2(b), where we see that the interference pattern positions of the real data compare extremely well to the simulation output. Figure 2(c) shows a close-up of the foil shadow region, where this time the simulation has a Gaussian broadening (full width at half maximum 38 μm) applied to account for source broadening of the XUV probe. We see that the fit is excellent (a 99.7% match across the foil shadow). Data from a 218-nm cold foil are also shown, highlighting the effect of some finite level of transmission (in this case ≈2.9%). The higher signal level is clear, with a modified structure due to interference between the transmitted and diffracted signals.

The harmonic generation of the XUV probe is prone to shot-to-shot variations in total energy and spatial distribution,

TABLE I. Measured transmission values. Errors are the resulting change in transmission after estimating the maximum and minimum incident XUV profiles deemed plausible in the foil shadow region, combined with the error margin in the diffraction simulation.

Al sample	Order	Energy (eV)	Transmission (%)	±Error (%)
cold 218 nm	11th	25.88	2.91	0.43
	13th	30.58	5.84	0.90
cold 418 nm	11th	25.88	0.96	0.15
	13th	30.58	2.42	0.36
heated 218 nm	11th	25.88	2.83	0.40
heated 418 nm	11th	25.88	1.01	0.15

yet our experimental arrangement did not allow for simultaneous measurement of the beam profile before transmission. However, from studying test shots with no sample in place, it can be seen that when a large peak structure is apparent in the XUV profile, the shape is typically Gaussian in nature. We find that by fitting Gaussian functions to the signal outside the shadow of the foil, we are able to predict the total energy under the peak in the foil shadow region to within ±15%. For this, the data from a test harmonic shot are compared to three fits: a target best fit and two fits deemed to be the worst case scenarios for an overestimation and an underestimation. The worst case estimations have a normalized χ^2 test value twice that of the target fit in the fitting regions. It is the largest source of uncertainty in the transmission measurements. By integrating the total signal detected in the foil shadow region and subtracting the signal calculated through the opaque diffraction simulation over the same limits, a value for the total transmitted signal can be found. The transmission values for the cold data shots are given in Table I.

The values in Table I include the effects of surface oxides and contaminants mentioned previously. These layers are extremely difficult to characterize or remove, but must be accounted for in any absorption measurement. We make the assumption here that the surface layers of each sample foil being probed are identical (all manufactured in the same manner, at the same time, in the same environment) and thus have identical transmissions. The following equation is used to calculate the absorption coefficient for each individual harmonic of frequency ω:

$$\alpha(\omega) = \frac{\ln[T_a(\omega)/T_b(\omega)]}{L_b - L_a}, \quad (1)$$

where T_a and T_b are the transmissions of the foils of lengths L_a and L_b, respectively. Ideally more than two different foil lengths would have been used, but the experiments are complex and difficult to implement and we were only able to obtain data for two sets of foils. The length values used here are the optical path length traveled by the probe through the sample foils. It accounts for the refraction of the signal due to the real part of the refractive index. The values used for calculating the deviation of the probe are close to unity for the 11th and 13th harmonic orders and are taken from Iglesias [6]. Unfortunately, for the 9th order, the real part of the index of refraction is much lower and the error margin in said value relates to a large fluctuation in the predicted absorption coefficient.

The absorption coefficients of the cold aluminium were found to be $2.47(\pm 0.69) \times 10^6$ and $2.44(\pm 0.68) \times 10^6$ m^{-1} for the 11th and 13th harmonics, respectively. The error bars are a combination of the error margins in the transmission measurements and the optical path lengths. These results are compared [see Fig. 4(a) later] to the theoretical models of Vinko *et al.* [5] and Iglesias [6] and the pre-existing experimental data sets of Keenan *et al.* [17], Gullikson *et al.* [18], CXRO [19], and Henke *et al.* [20]. Although the error margins are large, there is strong agreement with the values of Gullikson *et al.*, yet both theoretical models seem to predict much higher absorptions than those measured. It is true that the models discussed are not fully designed for cold material predictions. We focus our examination on the role of heating and the presence of a relative absorption change with raising sample temperature.

For heated foils, in addition to oxide and contaminant layers we should expect that there will be an expanded subsolid density plasma on either face of the heated foils. Hydrodynamic simulations were used to estimate the sample foil conditions upon heating with the well characterized palladium x-ray drive. For more information see Ref. [8]. The heating of the foils using this technique predominantly lies in a well understood photon range (3 keV), so the simulations should be reliable in estimating the expansion. For both heater foils, the x-ray yields observed by the crystal-based spectrometers on that shot, in combination with a blackbody model, were used to generate the photon flux source for HYADES modeling (a one-dimensional Lagrangian code) [21]. The density and electron temperature of the two shots being analyzed are shown in Fig. 3. One shot is a 418-nm foil, probed after 104 ± 5 ps, and the other is a 218-nm foil, probed after 108 ± 5 ps. The spatial coordinates of the 218-nm foil have been split along its center to move both edges to

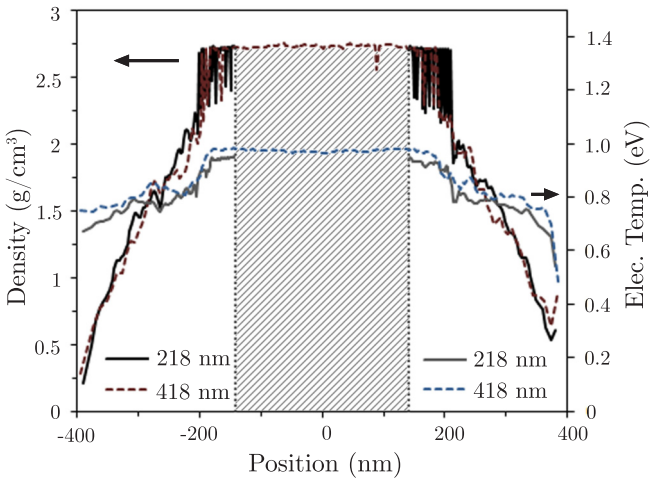

FIG. 3. Target sample conditions. Shown is a comparison of the 418-nm (dashed lines) and 218-nm (solid lines) target conditions, where the 218-nm foil has been split along its center and shifted to match the edge position of the 418-nm foil. The additional material of the 418-nm target is highlighted in crosshatching. The density and electron temperature are given by the left-hand and right-hand axes, respectively.

overlap those of the 418-nm target. The thickness of each foil is increased by $1/\cos 45^\circ$ to allow for the fact that the XUV probe penetrates the targets at 45°, with a corresponding increase in the presented foil thickness. The additional 283 nm of material (initial difference in thickness at 45°) in the 418-nm case has been highlighted in both plots. The heating in this region is extremely uniform, around $T_e \approx 1$ eV, and the foil remains at solid density at the time of probing. We assess the temperature dependence of the two absorption models being tested: the Iglesias model shows no increase in absorption until heating to over $T_e \approx 2$ eV, whereas the Vinko *et al.* model shows an increase in absorption immediately with heating, with approximately a 30% decrease in transmission already by $T_e \approx 0.1$ eV. For these reasons, we believe a sizable error in the sample temperature estimate (±80%) can be accommodated in this probing regime, where the absorption behavior change should still be measurable. We can also see in Fig. 3 that the expansion at the edges of the target foils is similar for both and note that any difference in target transmission should be due to only the additional central material of the 418-nm target. Although the classical absorption coefficient is not expected to be accurate in a great deal of the subsolid density plasma, we can use it to compare the two cases and see that the predicted absorptions are within 8% of each other [22]. This figure is used to estimate the potential error bar in assuming that the transmission of the expanded plasmas is equivalent for the two foil thicknesses.

The transmission values for both heated shots were found using the same method as that which was used for the cold foils. Table I details the measurements. Iglesias shows that the real part of the index of refraction value used to calculate the optical path length for the coefficient calculation should not change upon heating (below 10 eV). For the 11th harmonic the absorption coefficient was found to be $2.30(\pm 0.64) \times 10^6$ m^{-1}, similar to the cold foil value. The results indicate that upon heating the XUV absorption of the aluminium remains virtually unchanged. Unfortunately, a measurement of the 13th harmonic was not possible for either of the heated foils as the signal was below the detection limit. In Fig. 4(b) we compare the measured warm dense absorption coefficient, normalized to the measured cold value, to that of the Iglesias and Vinko *et al.* models (both of which are normalized to their cold absorption coefficient values). We note that by comparing the normalized absorption of cold and heated material, as the optical path length should not change, we should not be worried by any error in assuming the real part of the index of refraction. The result indicates that the Iglesias model more accurately predicts the behavior of the absorption upon heating.

In summary, upon heating, the absorption coefficient of $T_e \approx 1$ eV solid density aluminium remains very similar to its absorption under cold ambient conditions, for 25.9-eV photons (the 11th harmonic order). This is a significant result as the Vinko *et al.* model predicts an increase in the absorption coefficient of 40–70 % for these photon energies, whereas the Iglesias model predicts no change. Iglesias elaborates further on the possible source of the difference from Vinko *et al.* [23,24]. Using two different calculations for the electron-ion interaction, one based on the usual all-order interaction formula corrected for degeneracy and many-body screening

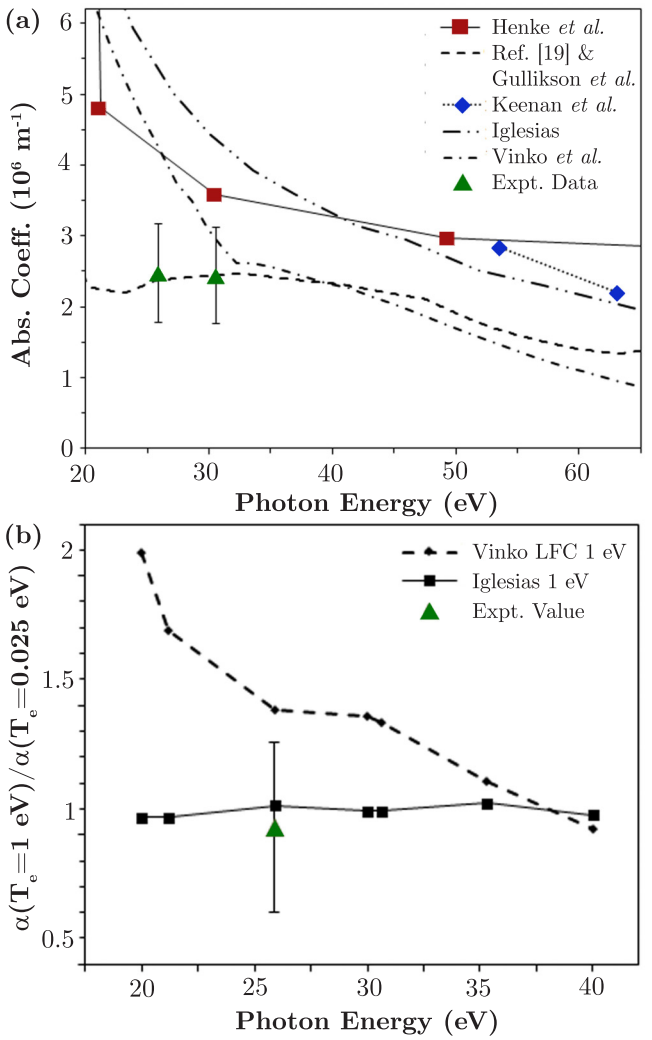

FIG. 4. (a) Measured absorption coefficients of cold aluminium (green triangles), compared to existing model predictions and experimental data. (b) Warm dense absorption coefficients (normalized to the cold values) compared to the normalized coefficients for both the Vinko *et al.* and Iglesias models under similar conditions (solid density, $T_e \approx 1$ eV). The errors bars were calculated using the standard combination in quadrature method ($\Delta E = \sqrt{\Delta A^2 + \Delta B^2}$, where ΔE is the resulting error and ΔA and ΔB are the errors in the two transmission measurements, respectively).

and another with a Born (or weak scattering) approximation, Iglesias suggests that the weak scattering approximation used by Vinko *et al.* may partly explain the discrepancy in the rate of absorption change with temperature. The increase in absorption with higher temperature (above $T_e \approx 4$–5 eV) in the corrected classical model is due to an increase in the many-body screening length and a reduction in the electron degeneracy. We have also observed that the measured absolute absorption coefficient is lower than both models discussed. Iglesias briefly suggests that including the dynamic response of the bound electron, instead of a frozen-core potential, may improve agreement. Further experimental measurements in the XUV photon region would be extremely useful in clarifying this discussion.

In conclusion, the experimental method described has proved effective in providing evidence to explore the two inverse bremsstrahlung models discussed. Further work, with a refined experimental method allowing for simultaneous input and transmitted profile measurement, though challenging, would provide greater insight into the true behavior of the collisional absorption of not only aluminium, but other low-Z materials.

This work was supported by the Engineering and Physical Sciences Research Council (Grants No. EP/I031464 and No. EP/I029206/1), European program COST MP1203, and the Science and Technology Facilities Council, United Kingdom. We acknowledge the support and contribution of the Target Fabrication Laboratory, Vulcan laser staff, and the Engineering workshop at CLF, RAL. Supplementary data and raw images are available at [25].

[1] M. Koenig *et al.*, Nucl. Fusion **44**, S208 (2004).
[2] N. Nettelmann, R. Redmer, and D. Blaschke, Phys. Part. Nucl. **39**, 1122 (2008).
[3] R. Ernstorfer *et al.*, Science **323**, 1033 (2009).
[4] S. Glenzer *et al.*, Science **327**, 1228 (2010).
[5] S. Vinko *et al.*, High Energy Density Phys. **5**, 124 (2009).
[6] C. A. Iglesias, High Energy Density Phys. **6**, 311 (2010).
[7] I. N. Ross *et al.*, IEEE J. Quantum Electron. **17**, 1653 (1981).
[8] B. Kettle *et al.*, J. Phys. B **48**, 224002 (2015).
[9] D. W. Phillion and C. J. Hailey, Phys. Rev. A **34**, 4886 (1986).
[10] D. Hemmers, M. Benzid, and G. Pretzler, Appl. Phys. B **108**, 167 (2012).
[11] R. Robinson, B.Sc. thesis, Brigham Young University, 2003, available at http://volta.byu.edu/pubs/RossCleaning.pdf.
[12] T. Ditmire, J. K. Crane, H. Nguyen, L. B. DaSilva, and M. D. Perry, Phys. Rev. A **51**, R902 (1995).
[13] C. G. Wahlström, J. Larsson, A. Persson, T. Starczewski, S. Svanberg, P. Salières, Ph. Balcou, and A. L'Huillier, Phys. Rev. A **48**, 4709 (1993).
[14] T. Kita, T. Harada, N. Nakano, and H. Kuroda, Appl. Opt. **22**, 512 (1983).
[15] E. Hecht, *Optics*, 4th ed. (Addison-Wesley, Boston, 2002).
[16] M. Born and E. Wolf, *Principles of Optics*, 4th ed. (Pergamon, Oxford, 1970).
[17] R. Keenan, C. L. S. Lewis, J. S. Wark, and E. Wolfrum, J. Phys. B **35**, L447 (2002).
[18] E. M. Gullikson, P. Denham, S. Mrowka, and J. H. Underwood, Phys. Rev. B **49**, 16283 (1994).
[19] Center for X-ray Optics, X-ray Database; http://henke.lbl.gov/optical_constants/
[20] B. L. Henke, E. M. Gullikson, and J. C. Davis, At. Data Nucl. Data Tables **54**, 181 (1993).
[21] J. T. Larsen and S. M. Lane, J. Quant. Spectrosc. Radiat. Transfer **51**, 179 (1994).
[22] L. B. Da Silva *et al.*, Phys. Rev. Lett. **74**, 3991 (1995).
[23] C. A. Iglesias, High Energy Density Phys. **7**, 38 (2011).
[24] S. M. Vinko, G. Gregori, and J. S. Wark, High Energy Density Phys. **7**, 40 (2011).
[25] www.qub.ac.uk/Research.